Heat management in solid free-form fabrication based on deposition by welding

Z Jandric and **R Kovacevic***
Research Center for Advanced Manufacturing, Department of Mechanical Engineering, Southern Methodist University, Richardson, Texas, USA

Abstract: Solid free-form fabrication (SFF) based on gas–tungsten arc welding (GTAW) is one of the few rapid prototyping techniques that has the capability to build three-dimensional metallic parts. For this application, a mild steel (AISI 1018) was used. The most important problem in this process was to find the optimal process parameters.

The goal is to build complex three-dimensional parts by depositing metal by welding in a form of layers. The building of a three-dimensional part by welding is especially sensitive to inadequate heat input. The traditional way of manually adjusting the heat input cannot be used because of the dynamic changes in the underlying substrate geometry. To investigate this problem a finite element model (FEM) has been developed that correlates the influence of the different underlying substrate geometry to the quality of the welding-based deposition process. The results from the FEM suggested that influence of the geometry is significant and cannot be neglected. Extensive experiments were designed and performed in order to verify the conclusions derived from the results of the FEM. A real-time adaptive controller of the welding parameters is proposed. This controller performs heat management in real time according to the volume changes of the material of the underlying layers in the vicinity of the heat source. In addition, the overall system performance was monitored and recorded by through-the-arc sensing in order to demonstrate the versatility and robustness of the controller.

Keywords: heat management, gas–tungsten arc welding (GTAW), finite element model, controller

1 INTRODUCTION

Several methods have been proposed and utilized for creating three-dimensional objects by the incremental material build-up of thin layers. The most common processes are stereolithography, laser-engineered net shaping (LENS), lamination, selective laser sintering, ballistic powder metallurgy, three-dimensional printing and near-net thermal spraying [1].

None of the aforementioned layered fabrication techniques has been successfully used to make quality metallic parts. Only laser sintering and the ballistic particle manufacturing have been proposed for metallic part fabrication. However, the objects made by these techniques are porous, have weak bonds between layers and, consequently, have structural weakness.

Three-dimensional parts built by the solid free-form fabrication (SFF) based on deposition by welding exhibit excellent properties. They could be built from the metal; they are porous free but yet have very good bonding between all the layers. This technique satisfies the increased needs that are required today, for the quality metallic parts are produced in a timely manner directly from the three-dimensional solid models [2, 3].

SFF deposition based on welding is a layered manufacturing process that builds physical objects by depositing material selectively layer by layer under computer control. The outer geometry of the object and the interior material distribution are simultaneously realized in this process. The welding process for building three-dimensional parts was mentioned for the first time in 1925 by Baker to produce receptacles or containers of ornamental and useful shapes [4]. The first known application of SFF based on deposition by welding was reported in Germany in the 1960s when several free-standing shapes were built. Among the first in this area were Babcock and Wilcox, for building large components from austenitic materials, and Rolls–Royce, who

tried to reduce the component costs by reducing the level of waste of high-performance alloys [5]. A number of researchers [6–15] contributed in developing this process, although they were mainly concerned with the equipment set-up and possible applications, and less with the problems met in the process.

Recent development of this technique has been achieved by several research teams at the University of Nottingham, UK [16, 17] (adapted spiral overlay welding using multiple beads to enable the production of parts wider than normally possible from a single bead, and concentrated on the building of sloping surfaces so that the molten welding material does not flow off its desired position before it has solidified), researchers from the University of Minho, Portugal, and University of Wollongong, Australia [18] (built different three-dimensional parts, such as a chimney-shaped part, a bow-tie-shaped part, and a pint-glass-shaped part), United Technologies Pratt and Whitney [19] (investigated weld process control and developed a programmable controller that can be used to control the major process parameters, such as current, velocity and wire-feeding speed), the Fraunhofer Institute for Production Systems and Design Technology, Berlin, Germany [20] (concluded that SFF based on deposition by welding has the potential to optimize product development if it is embedded into the process chain), the Korean Institute of Science and Technology and Hong Kong University [21] (combined a five-axis milling machine with the welding process not only to increase both the dimensional accuracy and the surface quality of the three-dimensional metallic parts but also to show the great manufacturing flexibility of this SFF technique) and the Southern Methodist University (SMU), Dallas, Texas, USA [22] [proposed a system for SFF based on deposition by gas–metal arc welding (GMAW) and gas–tungsten arc welding (GTAW) that addresses the challenge of a simultaneous geometric regulation of the dimensional tolerances and mechanical properties of the part, by combining heat and mass transfer control].

In this paper, a new parameter called the geometrical factor will be introduced, the modelling of the SFF based on deposition by GTAW will be presented, the results will be experimentally verified and the new heat input controller will be presented with the final goal of controlling the input energy so that the uniform beads can be deposited regardless of the underlying substrate geometry.

2 SMU'S SFF BASED ON DEPOSITION BY WELDING

Although initially SMU's research team used GMAW for deposition, GTAW-based metal deposition prevailed because of a number of advantages. The advantages of GTAW include the following: the wire-feeding speed is independent of the current; the presence of the deposited bead has no influence on the arc stability, so that beads can be partially (or fully) overlapped, and a very smooth top surface is obtained as a result; there are no spatters, and so it is not necessary to mill off the top surface after each deposited layer, which speeds up the process; the wire is fed directly to the molten pool, and the molten material is evenly spread by the surface tension that produces the void-free material deposition. It has already been demonstrated that by using GTAW very complex shapes can be built [2, 3, 23]. To make GTAW even more suitable for SFF, a heat management, i.e. a balance of the input and output energy should be maintained during the deposition process in order to obtain a uniform geometry of the weld bead across the deposited layer. In addition, controlled heat input should endow deposited material with a homogeneous crystallization and phase transformation.

Until now, static welding parameters were used during the layer deposition. The parameters were adjusted to provide good or rather acceptable overall process quality. The quality of the process is judged visually by inspecting the layer smoothness, i.e. evaluating the possibility for depositing the next layer without milling off the previously deposited layer. It was noticeable that the quality altered mostly in the vicinity of the external and internal boundaries. Welding parameters were chosen according to the recommendations designed for traditional welding. These recommendations considered the temperature distribution where the heat transfer conditions around the heat source were uniform (Fig. 1, point I). At point I, from Fig. 1, the heat is conducted through the substrate in all directions within the observed half-sphere. If any other marked point of this figure is observed, it can be seen that heat transfer conditions are very different. Thus, at point III (45° angle), only one-eighth of the material around the point exists. As a result, the heat is conducted only within one-eighth of the half-sphere. By using the same logic in the SFF based on deposition by welding, especially when material is deposited along the boundaries and in their vicinity, the heat transfer conditions alter.

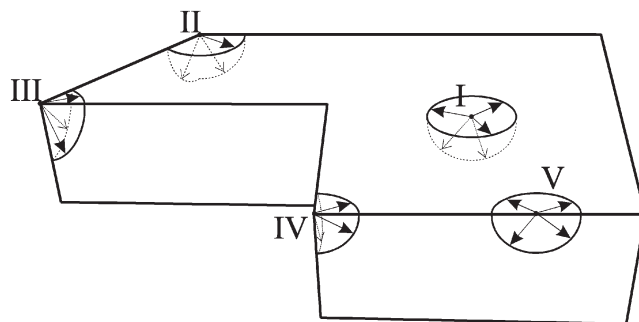During the making of the three-dimensional parts, it has been learned that the welding process parameters

Fig. 1 Volume of the heat sink at different substrate points

Proc. Instn Mech. Engrs Vol. 218 Part B: J. Engineering Manufacture

B19003 © IMechE 2004

cannot be constant if a uniform layer is desired. What makes this problem much more difficult than it appears is that the parameters must be suitable for every point in the layer. Namely, when a two-dimensional cross-section of a three-dimensional part with complex external and/or internal geometrical features is observed, it is clear that the surrounding area of almost every point is different. If the fact that these points cannot be considered just in a two-dimensional manner is also considered, since previously deposited layers can also have different cross-sections, it is apparent that the welding conditions alter for each point. Welding conditions, i.e. heat transfer conditions, are different for different geometries. In reality, it is difficult to determine the extent to which the underlying geometry influences the depositional process, and how distant the boundaries should be so that their influence can be neglected. One way to quantify the effect is through extensive experimental research. Another way is through process modelling.

If the experiments are well prepared, then the results will be immediately forthcoming. However, in order to study the effect of the underlying geometry on the selection of the major welding parameters (welding speed, wire-feeding speed and welding current) the number of experiments becomes enormous. To prepare and perform such a large number of experiments is both time consuming and expensive. Furthermore, different filler metals, base metals and various other conditions will result in an endless repetition of the experiments.

Another way to understand the influence of the different heat transfer conditions on the welding process is by modelling the process. A substantial amount of research has been documented for modelling and understanding the welding process. Rosenthal [24] and Rykalin [25] developed a solution to the heat equation for point and for line heat sources on idealized geometries such as infinite plates. Because of the computational difficulties encountered when attempting to include inelastic strains in an analysis in which rapid temperature changes take place, some analytical work was carried out that goes beyond Tall's one-dimensional analysis of longitudinal stress [26]. Several researchers have attempted to use a more realistic distribution of heat source [26–28], but none has solved the entire temperature field for a travelling distributed source. A determination of the complete thermomechanical response due to welding requires a full three-dimensional inelastic analysis of mechanical behaviour, accompanied by a computation of the three-dimensional transient temperature distribution. In the last decade, models for non-linear transient finite element heat transfer analyses of the welding process have been developed [29–33].

Numerical modelling requires initially considerable time and effort to build geometry, to mesh it appropriately, to set boundary conditions, to set temperature-dependent material properties and to programme the path of the heat source but, once the model is obtained,

it is easy to change any welding parameter, welding conditions and type of material. The objective of this numerical model is to offer a better understanding of the process, and how bead geometry, the molten pool and heat-affected zone (HAZ) are related to the changes in the volume of the heat sink. Also, once the model is set properly, the modelling results can be used for the prediction of the appropriate parameters for different heat transfer conditions. In this way, the number of experiments can be significantly decreased, which can reduce experimental costs and save time. For this purpose, the temperature distribution in the three-dimensional model with the different geometrical features, which represent different heat transfer conditions, will be investigated. As opposed to the Rosenthal solution, this model does not neglect convection heat losses; it considers the moving heat source in time. Also, the heat source has a Gaussian heat distribution, and all the material properties are temperature dependent. In this paper, the welding process is numerically modelled by using a finite element method.

3 WELDING PROCESS

3.1 Physics of GTAW

The GTAW (Fig. 2) process is used with a shielding gas, without the application of pressure. To start the arc, a high voltage is used to break down the insulating gas between the non-consumable electrode and the workpiece. The electric arc is produced by a passage of current through the conductive ionized shielding gas. Current is then constantly transferred through the electrode to keep the electrode arc. The metal to be welded is melted by the intense heat of the arc and fuses together with the filler material. Once the arc and weld pool are established, the torch is moved, and the arc progressively melts the substrate surface and filler metal. Besides the equipment, the most important aspects of the GTAW process are the welding process parameters. To achieve a specific weld quality and production output, suitable welding parameters must be used. The important parameters are the welding current, arc voltage, wire feeding speed, welding speed, type and purity of the shielding gas, shielding gas flowrate, electrode-to-substrate angle, arc length, electrode tip geometry, substrate surface conditions and tungsten electrode material.

3.2 Geometrical factor as a connection between welding parameters and substrate geometry

It has already been mentioned that an obvious difference exists when the welding is applied for the fusion of two parts together and when it is applied for the fabrication of the three-dimensional parts. That difference is
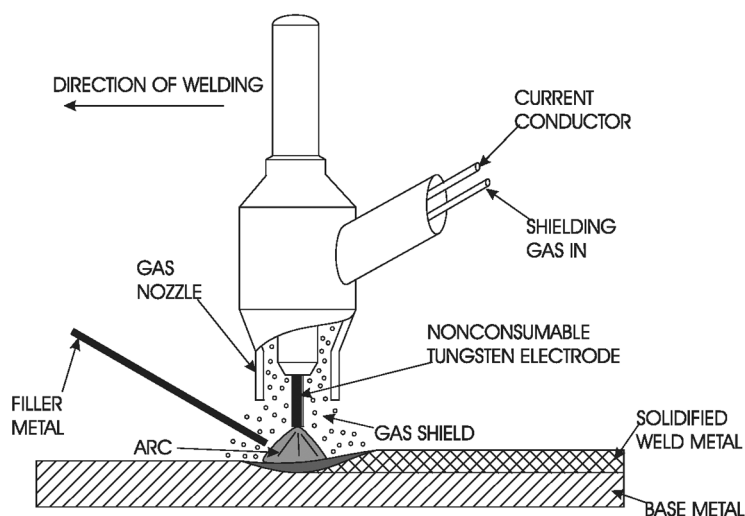
Fig. 2   Gas–tungsten arc welding process

especially pronounced when the bead is deposited along the part's boundaries and in their vicinity. The final goal is to be able to control the welding parameters in order to achieve deposition of the uniform beads throughout the layer. That goal will not be difficult to achieve if the heat transfer conditions in the vicinity of the heat source do not change within the layer. Since this is not the case, the constant heat source produces the beads with different geometries and different HAZs. Namely, the input energy is spent for melting the feeding wire, melting the substrate material, and the rest is conducted through the material (see the discussion on the balance of energy in the mathematical modelling section 6.1). The amount of energy spent for melting the feeding wire is constant. Thus, to have uniform deposition, it is only necessary to secure the use of an adequate amount of energy for melting the substrate. The goal is to obtain an equal depth of the HAZ independently of the location of bead. Therefore, it is necessary to describe mathematically where the influence of the volume of the heat sink exists and what the level of the influence for each observed location is. For this purpose, a new geometrical factor ξ_G is introduced. The geometrical factor is a dimensionless parameter with possible values from 0 to

1. The geometrical factor has the value of 1 when the observed point is remote from the part's boundaries. As the point approaches the boundaries, the value becomes smaller. Thus, the geometrical factor represents the actual amount of the material in the heat sink (around the observed point). The geometrical factor reflects the influence of the volume of the heat sink. In order to calculate this value, the following four steps should be completed:

1. Create a solid model.
2. Create a three-dimensional matrix.
3. Calculate a geometrical factor.
4. Generate the two-dimensional matrix for each layer to be deposited.

The first step is to design the three-dimensional solid model (Fig. 3) by computer aided design software. The three-dimensional solid part should have all the details of the wanted part (Fig. 4), so that the model is as realistic as possible.

The second step is to digitize the volume by creating the matrix of voxels that are denoted by the 'ones' and the 'zeros' (Fig. 5). 'Ones' mark the voxels where the material in the solid model exists, and 'zeros' mark the voxel where the material does not exist. The matrix of
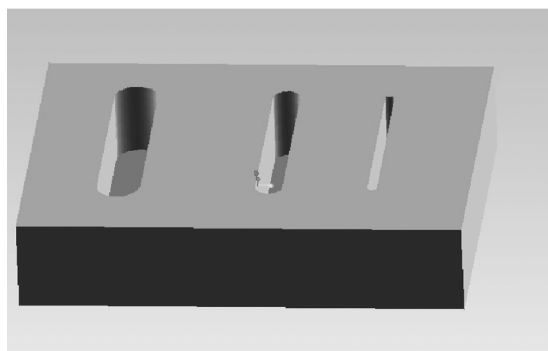

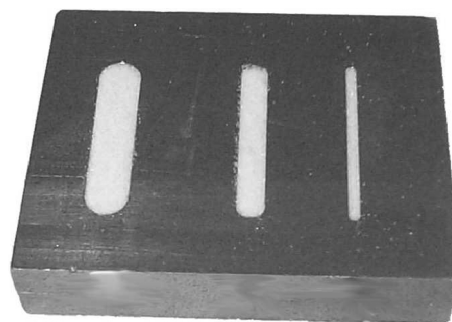Fig. 3   Three-dimensional solid model
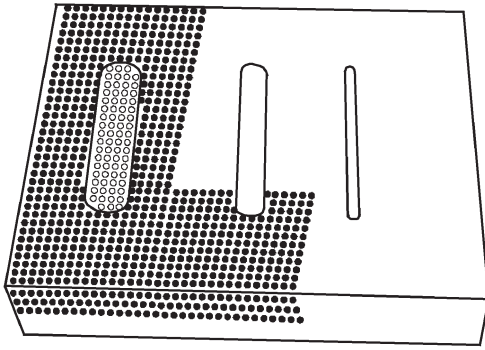

Fig. 4   Built three-dimensional part

Fig. 5 Part as a matrix of 'ones' (●) and 'zeros' (○)

Fig. 6 Welding over the channels

voxels is determined by its resolution defined as the number of the voxels within the unit length.

The third step is computationally most demanding. For each voxel in a three-dimensional matrix the geometrical factor ξ_G, is calculated. The calculation of the geometrical factor is based on the fact that the HAZ for a weld on a semi-infinite solid is theoretically half of the sphere [24]. The size of the radius R of the half-sphere is thus experimentally obtained. Namely, from the bead with the most suitable geometry the HAZ is measured, and that value is adopted as the size of the radius. It is worth noting here that the radius R remains constant, while the heat input changes after the geometrical factor and allows R to stay the same for each instance. The centre of the sphere is the point (which is the centre of the observed voxel) for which the geometrical factor is to be calculated with the coordinates (x_c, y_c, z_c). All the centres of the voxels in the range ($x_c \pm R$; $y_c \pm R$; $z_c - R$) are checked for their distance d from the half-sphere centre according to

$$d = \sqrt{(x_c - x)^2 + (y_c - y)^2 + (z_c - z)^2}$$

$$d \leqslant R \tag{1}$$

Thus, x, y and z are the coordinates of an arbitrary centre of the voxel. Further, all the voxels that satisfy $d \leqslant R$ are counted, where the counter is denoted by V_{max}, and all voxels with value 1 that satisfy $d \leqslant R$ are counted with the counter denoted as V. The geometrical factor can
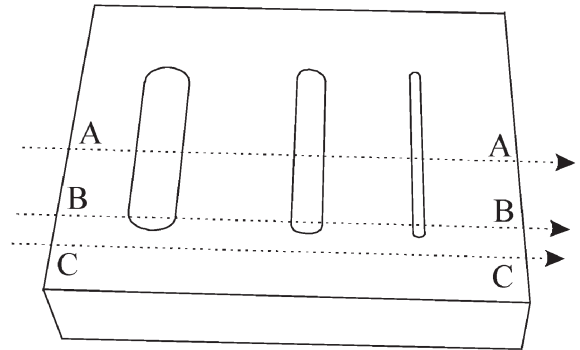
be defined as

$$\xi_G = \frac{V}{V_{max}} \tag{2}$$

where the geometrical factor is the ratio of the volumes, where V_{max} is constant and depends on the predetermined radius of the half-sphere and where V is a variable and depends on the volume of the heat sink in the surrounding of the observed voxel. Here, the volume is digitized; therefore, the model error is inherited. However, it should be noted that this off-line heat input planning model allows the matrix resolution to be increased by up to virtually any value.

The fourth step extracts all geometrical factors from the three-dimensional matrix of the geometrical factor with the same z^* coordinate in a unique two-dimensional matrix that will be used when the layer with a z^* distance from the base plate is deposited. As an example, a few diagrams with the calculated values of the geometrical factors along the directions A–A, B–B and C–C (from Fig. 6) are shown in Figs 7a, b and c respectively. These diagrams are obtained for the top layer, where the bottom of the channels is sufficiently remote and does not have any influence on the geometrical factor.

3.3 Balance of energy in the welding process

To recall, any change in the welding process will affect the bead geometry, i.e. the bead width, the bead build-up,
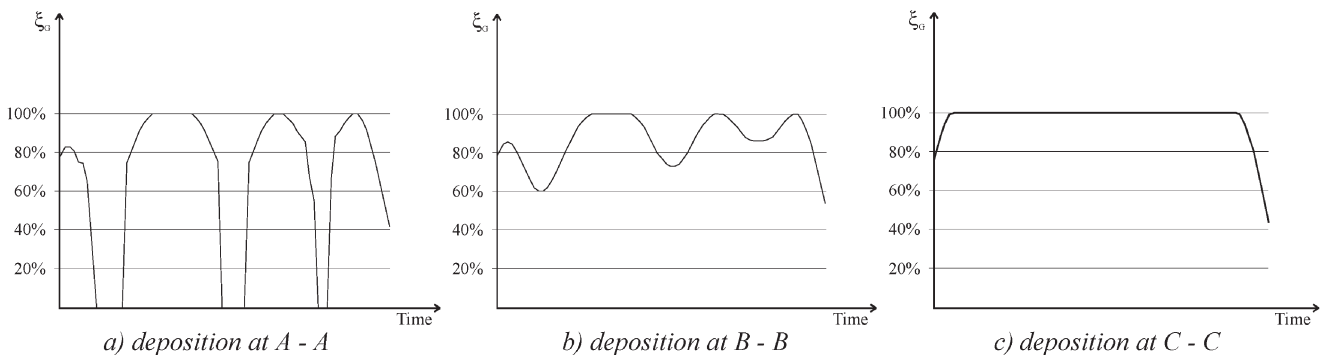

a) deposition at A - A

b) deposition at B - B

c) deposition at C - C

Fig. 7 Calculated geometrical factor

the depth of penetration and also the HAZ. As a whole, this process can be summarized as a balance of energy [34]. The net energy delivered to the workpiece is basically distributed in two ways; a portion is used to melt the fusion zone while the remainder is lost to the adjacent base metal around the fusion zone primarily by thermal conduction. The energy lost to the base metal around the fusion zone contributes to the formation of the HAZ and heating of the base metal above the ambient temperature. The total energy balance can be expressed as

$$E_{arc} + E_{electrode} = E_{losses} + E_{fusion\ zone} + E_{base\ metal} \quad (3)$$

The left-hand side of equation (3) represents the total energy generated by the process. E_{losses} represents losses to the environment that are quantified by the arc efficiency factor. $E_{fusion\ zone}$ represents the energy used for melting the fusion zone, and the $E_{base\ metal}$ represents the energy lost to the surrounding base metal. To obtain any particular welding result, the energy used in the fusion zone must be balanced with the energy lost to the surrounding base metal.

4 FINITE ELEMENT MODELLING OF THE HEAT TRANSFER IN WELDING-BASED DEPOSITION

4.1 Heat transfer governing equations

In heat transfer modelling the energy is considered and stress, strain and displacement are ignored [35]. The temperature $T(x, y, z, t)$, as a function of spatial coordinates (x, y, z) and time t, satisfies the following parabolic differential equation, which is the heat equation, at every point in the domain D:

$$\frac{\partial}{\partial x} k_x \frac{\partial T}{\partial x} + \frac{\partial}{\partial y} k_y \frac{\partial T}{\partial y} + \frac{\partial}{\partial z} k_z \frac{\partial T}{\partial z} + Q$$
$$= \rho c \left(\frac{\partial T}{\partial t} - v \frac{\partial T}{\partial x} \right) \quad (4)$$

where (x, y, z) are the coordinates, t (s) is the time, $Q(x, y, z, t)$ (W/m^3) is the source or sink rate of heat, k_x, k_y and k_z (W/m °C) are the thermal conductivities in the x, y and z directions respectively, c (J/m^3 °C) is the volumetric specific heat, ρ (kg/m^3) is the density, v (m/s) is the velocity of the workpiece and T (°C) is the temperature.

If k or c are functions of temperature T, equation (4) is non-linear. On the boundary of D, either the essential boundary condition or the natural boundary conditions must be satisfied. The essential boundary condition can be defined as

$$T(x, y, z, 0) = T_{amb}(x, y, z, t) \quad (5)$$

on the boundary S_1, i.e. $(x, y, z) \in S_1$: $t > 0$. S_1 represents the bottom of the holding plate. This condition prescribes the nodal temperatures at the bottom of the holding plate, where the temperature is controlled by the liquid cooler. The natural boundary conditions can be defined as

$$k_n \frac{\partial T}{\partial n} + q + h(T - T_0) + \sigma \varepsilon (T^4 - T_0^4) = 0 \quad (6)$$

on the boundary S_2, i.e. $(x, y, z) \in S_2$: $t > 0$. S_2 represents those surfaces that are subject to radiation, convection and imposed heat fluxes. In the model it is assumed that the distance between the electrode and the substrate (arc length) is constant and that the applied heat source is closely approximated by the Gaussian distribution

$$q^* = \frac{k}{\pi} q\, e^{-kr^2} \quad (7)$$

where q (J/s) is the effective output of the heat source, k (mm^{-2}) is a factor designating the heat source concentration (i.e. with the Gaussian distribution curve) and r (mm) designates the distance from the centre within a circular source. The constant heat source is applied on the surface of the quadrilateral mapped mesh. Namely, the local cylindrical coordinate system is moved along the wanted path and the nodes within the radius $r = 2.5$ mm are selected. Depending on the distance of the node from the centre of the heat source, different levels of the heat source are applied. In this case, all surfaces, except for the bottom of the holding plate, are subject to convection, and the top surface is additionally subject to the heat fluxes.

Other symbols are defined as follows: $q(x, y, z, t)$ (W/m^3) is a prescribed heat flux normal to S_2, k_n (W/m °C) is the thermal conductivity normal to the surface, h (W/m^3 °C) is the heat transfer coefficient for convection, T_0 (°C) is the ambient temperature for convection and/or radiation, σ is (=5.67 × 10^{-8} W/m^2 °C^4) is the Stefan–Boltzmann constant for radiation and ε is the emissivity (the full amount of energy emitted per square metre of a black body per hour).

If radiation is included or if the convective heat transfer coefficient is temperature dependent, this boundary condition is non-linear. The initial condition is

$$T(x, y, z, 0) = T_0(x, y, z) \quad (8)$$

where the initial condition must be specified for $(x, y, z) \in D$. The inclusion of temperature-dependent thermophysical properties and a radiation term in the above boundary condition makes this type of analysis highly non-linear. In this model the temperature distribution is needed, losses by convection are included and the radiation effects are neglected. To provide data for the heat capacity matrix and for the heat conduction matrix, temperature-dependent material properties for
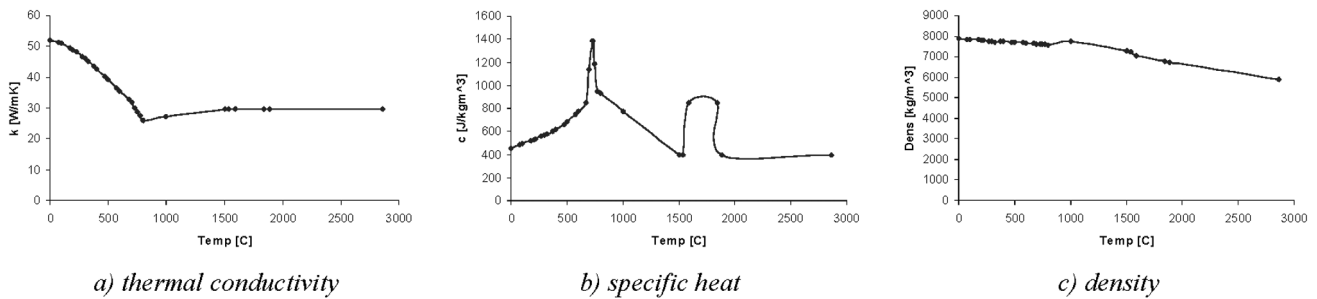
a) thermal conductivity b) specific heat c) density

Fig. 8 Temperature-dependent material properties

thermal conductivity, density and specific heat are included. The numerical values of the thermophysical properties are selected according to references [**36**] and [**37**] and their dependences on temperature are given in Fig. 8.

If in the partial differential equation (4) the boundary conditions of equations (5) and (6), and the initial condition of (8) are consistent, the problem is well posed and a unique solution exists.

4.2 Problem definition

Figure 9 shows a physical model that was selected for studying the effect of the welding parameters. This shape was chosen so that the majority of the possible heat transfer conditions were covered. The smallest angle at this workpiece was 45°. Also, only six different angles (heat transfer conditions) were chosen, because the equivalent experiments were performed as well, and each angle was cross-sectioned, polished and chemically treated. The dimensions of the part on which the welding was performed in the x, y and z directions were 100, 25 and 50 mm respectively. It was estimated that the height of 25 mm was large enough that there was no influence of the holding plate on temperature distribution in the vicinity of the heat source. The base material was AISI 1018 steel.

The welding speed is 3.81 mm/s. The diameter of the moving heat source is chosen to be 5 mm. Its value is

determined experimentally as the diameter of the HAZ along the E–F path (see Fig. 9) from the experiment which yields the most appropriate size and shape of the deposited bead from layer deposition point of view. In order to calculate the level of the heat source, the well-known expression for energy generated by the arc that is given simply by the product of welding current and welding voltage is first considered, but only net energy is delivered to the substrate. The calculation of the net energy requires knowledge of the arc efficiency. Therefore, it is important to know the arc efficiency of the welding process in order to utilize accurately the temperature distribution in the heat flow model. An accurate calculation of the arc efficiency has been made by Radaj *et al.* [**34**] and, for the GTAW process, this calculation has an average value of 0.67 ± 0.05. It is approximated as 0.7 in the modelling presented in this paper.

The following assumptions have been made in the formulation of the finite element model:

1. The heat input remains constant during the process. (In reality, fluctuations in the current and voltage cannot be avoided. Therefore, to minimize the error, the mean value is used.)
2. The workpiece is at a uniform temperature before the welding process starts.
3. The body is exposed to a uniform forced convection.
4. The surface-to-surface contact between the workpiece and 'support plate' is ideal; thus, heat is transferred by conduction throughout the whole contact area.
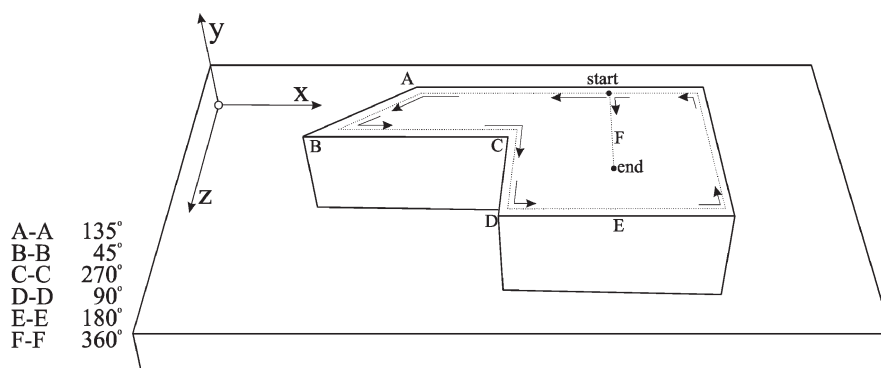

A-A	135°
B-B	45°
C-C	270°
D-D	90°
E-E	180°
F-F	360°

Fig. 9 Geometry of the physical model

5. The effect of gas diffusion in the weld pool has not been considered.
6. All thermophysical properties are considered to be temperature dependent.

4.3 Formulation of finite element model

In this study, the commercial finite element software ANSYS has been used. It provides a convenient means of numerically modelling the welding process. The model is discretized into individual finite elements that collectively approximate the shape of the model. A three-dimensional thermal solid element type with a three-dimensional thermal conduction capability is used. The element has eight nodes with a single degree of freedom and temperature at each node. The element is applicable to a three-dimensional, steady state or transient thermal analysis.

In the developed model, 'mapped' mesh was mostly used so that the mesh has a regular pattern with obvious rows of elements. Also, a transition-mapped hexahedral meshing was used by specifying line divisions on the side edges of the volume such that the divisions permit a transition-mapped hexahedral mesh. Thus, the elements at the top layer of the substrate are defined with a significantly smaller height than the elements at the very bottom of the substrate (Fig. 10). This definition is made because the temperature gradient in the vicinity of the top surface where a heat flux is applied is much higher.

For this model the thermal fields and thermal history are required; therefore a transient thermal analysis must be performed. This analysis requires an integration of the heat conduction equation with respect to time. The basic finite element model equation for the thermal problem can be derived from the thermal equilibrium equation

$$[C(T)]\{\dot{T}\} + [K(T)]\{T\} + \{V\} = \{Q\} \qquad (9)$$

where $[C] = \int_V \rho c[N][N]^T \, \mathrm{d}V$ is the heat capacity matrix, $[N]$ is the shape function matrix, $[K_T] = \int_V k[B][B]^T \, \mathrm{d}V$ is heat conduction matrix, $\{T\}$ and $\{\dot{T}\}$ are the nodal–temperature vector and the nodal–temperature–rate vector respectively and $\{Q\}$ is the heat-flux vector. To obtain the solution the direct elimination solver, the sparse direct solver, is used.

5 MODELLING RESULTS AND MODEL VERIFICATION

5.1 Temperature fields

The temperature fields, i.e. isotherms, obtained with the three-dimensional thermal analyses for different time intervals are given in Figs 11a to f. Points of interest are located where the surrounding mass of the material varies between 12 and 100 per cent of the maximum possible (points are indicated with the letters A to F; see Fig. 9). The heat input is kept constant and moves across the top surface at a steady rate. In the model, the heat flux travels at speed of 3.81 mm/s. From Fig. 11, the temperature change with different heat transfer conditions can be observed. Consequently, the size of the molten pool and the size of the HAZ alter as well. The central temperature contour in each image represents a critical temperature of 1530 °C as the melting temperature of AISI 1018 steel. Hence, this contour represents the boundary of the molten pool.

These results were subject to further investigation. Several experiments were performed where the workpiece was of the same material and with the same geometry as the three-dimensional model's geometry. Also, process parameters such as the welding current and welding speed have equivalent values to those used in the model. Thus, in the experiment the following parameters are used: the welding current is 80 A, the welding speed is 3.81 mm/s, the diameter of the feeding wire is 0.9 mm, the wire feeding speed is 13.33 mm/s and the arc length is
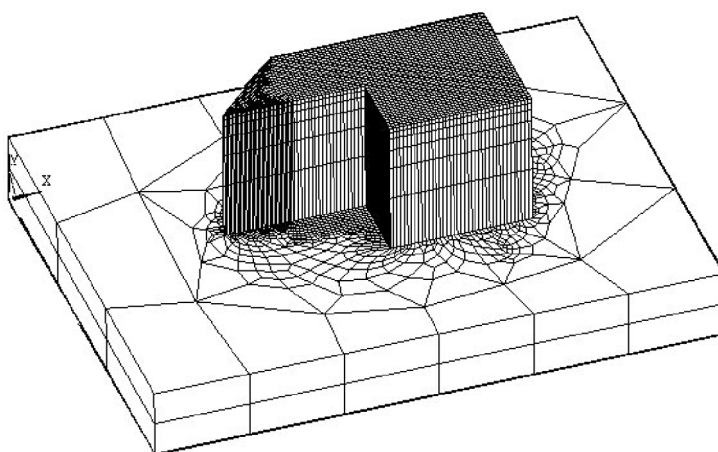

Fig. 10   Meshed three-dimensional finite element model
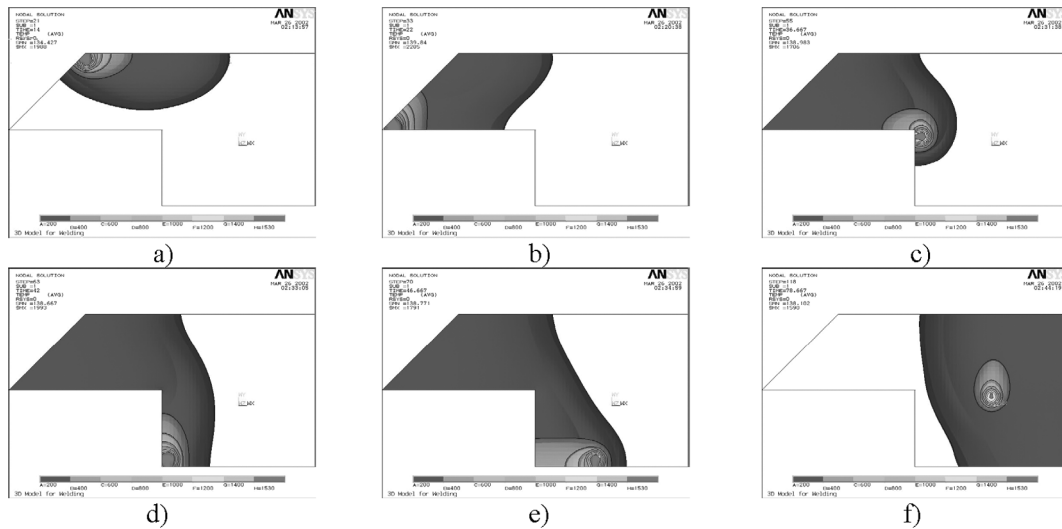
Fig. 11   Temperature fields as a function of volume of heat sink

kept at 2 mm. Pure argon is used as the shielding gas, and the shielding gas flowrate is 236 mm^3/s.

5.2   Model verification with coaxially integrated camera

From the temperature contour figures, the sizes of the molten pool are extracted and compared with their equivalents recorded from the experiments (Table 1 and Fig. 12). For this purpose, a high-resolution charge-coupled device (CCD) camera (8 bit, 640×480 pixels and 30 frames/s) integrated coaxially with the torch is employed. Images of the molten pool from the model and experiment are scaled to fit into the table window, and next to each image is the numerical value of the molten pool geometry at the top surface. The numerical values are shown in Fig. 12, from where it can be seen that the molten pool geometry at the top surface obtained from the model is in good agreement with the molten pool geometry at the top surface recorded from the experiments.

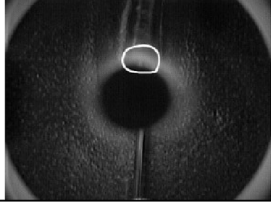## 5.3   Molten pool and corresponding HAZ
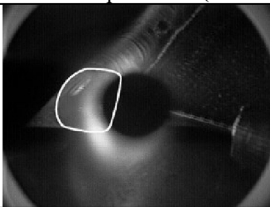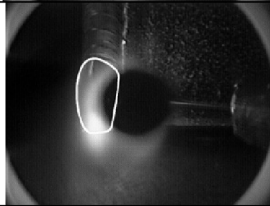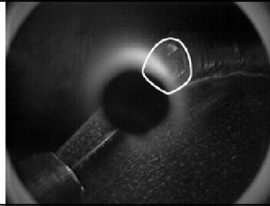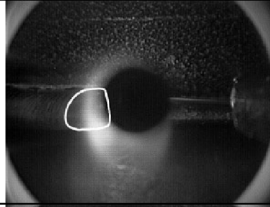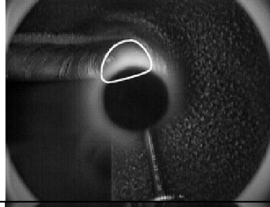
If the temperature fields are further observed; it can be seen that, as expected, the highest temperature is achieved in the 45° corner, since it is the corner with the smallest volume of the heat sink. In Fig. 13 is shown a 45° corner together with the molten pool and HAZ. The molten pool and HAZ are obtained from the finite element model by showing the thermal iso-surfaces at the melting temperature (1530 °C) and at the initial recrystallization temperature (727 °C) respectively. In Fig. 13a, the heat input is far from the corner (45°); therefore, the volume of the heat sink is half the maximum possible. At this instant, there is barely enough heat to melt material and, consequently, a small molten pool is formed. In Fig. 13b, the heat

input is closer to the corner, the volume of the heat sink is decreased and the amount of the melted material is enlarged. In Fig. 13c, the heat input is placed above the corner itself. The volume of the heat sink is four times smaller than in the first case and, as a result, the molten pool and HAZ are enlarged. Similar analyses are performed for all other edges but, before any conclusions were derived, these results are compared with results from the experiment.

5.4   Model verification by cross-sections of weld beads

After depositing beads along the edges of the polygon by applying the constant heat input, as in the finite element model, they are cross-cut along the symmetry of the angles at point A, B, C, D, E and F (see Fig. 9) in order to obtain information about the weld bead geometry. Then, each cross-section was polished to a 1 μm finish and etched in a 2 per cent Nital solution. These cross-sections are shown in the left-hand column of Table 2. In the middle column of Table 2 are shown modelling results, i.e. the model prediction. Here, only isotherms that represent boundaries of the molten pool and HAZ are shown. Images from the left-hand and the middle column are first scaled to the same size and then overlapped. In this way, the boundaries of the molten pool and HAZ obtained experimentally and by modelling can be directly compared. The boundaries of the molten pool are well anticipated, and only at angles of 180° and 270° are small differences noticed. At an angle of 180°, the bead is deposited closer to the edge which is caused by the mistake in programming the torch path and, as a result, the depth of penetration in the experiment is larger. At an angle of 270°, there is also a small difference in the anticipated depth of penetration. Also, it should be noted that the predicted HAZ seems much larger than the HAZ obtained from

Table 1   Images acquired with coaxially integrated camera versus modeling results

Angle	Experiment (Area×10⁻⁶ m²)		Model (Area×10⁻⁶ m²)	
45°		14.8		16.82
90°		11.8		12.58
135°		8.9		11.47
180°		7.1		11.08
270°		7.0		4.04
360°		3.9		0

the experiments. The actual difference is smaller than could be concluded from these images, because the predicted boundary of the HAZ is where the first changes in the structure occur, and they are not visually obvious.
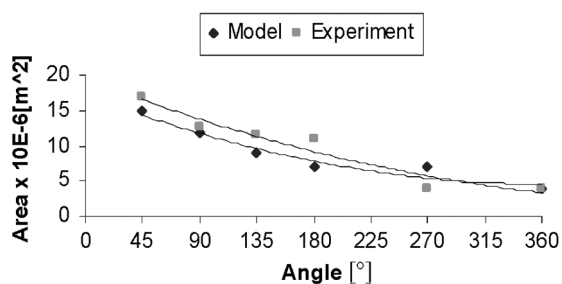
Fig. 12   Model versus experimental results

Namely, there is a just a slight difference in colour between the material that was exposed to the temperature above 727 °C and the material that was not heated to this temperature. It is known that human eyes are not sensitive to grey colours. However, it can be seen that the shape of the predicted HAZ follows the shape of the experimentally obtained HAZ boundaries. Thus, the model can be used reliably for the prediction of the size of the molten pool and HAZ.

5.5   Model verification by employing thermocouples

Nevertheless, these 'large differences' in the predicted HAZ opened a discussion on how real the obtained temperatures were. To be sure that those temperatures
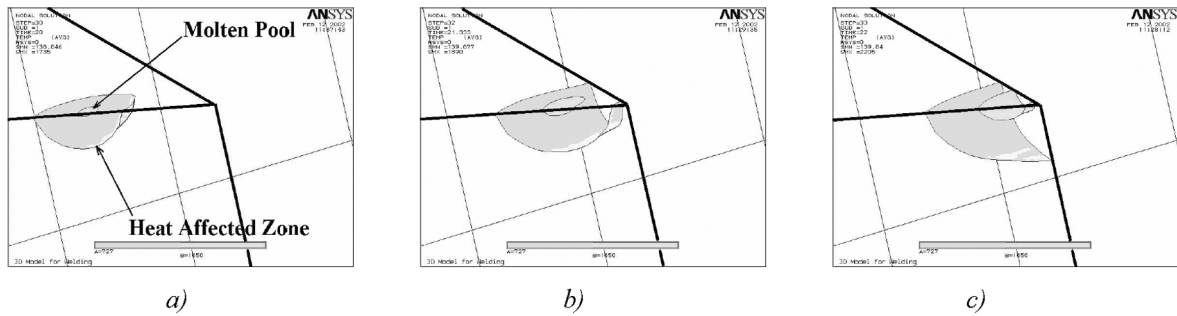
Fig. 13 Influence of the geometry on the size of the molten pool and the HAZ

obtained by the model represent the real temperatures, additional experiments were conducted. The temperature history from the model is verified experimentally by employing the thermocouples (Fig. 14). K-type NiAl–NiCr thermocouples are used. For each thermocouple, a hole is drilled at the appropriate location. Each hole is drilled vertically from the bottom towards the top of the sample. The depth of each hole is 1.5 mm less than the height of the sample. At the bottom of each hole is placed thermally conductive and electrically insulating high-temperature cement in order to isolate thermocouples from noise originating from the arc. The thermocouples and thermally conductive cement are inserted together and left for the cement to be cured. In order to compare the temperature history from the model with experimental results, nodes that are 1.5 mm beneath the top surface from each corner are selected. The temperatures from the model for all angles of the polygon are recorded in time (Fig. 15). It could be seen that smaller volume of heat sinks achieve a much higher temperature. These results also agree well with the modelling results obtained by Kamala and Goldak [**38**], who also showed that the temperature increases when the heat flux is approaching a smaller volume of the heat sink. Direct comparisons of experimental and modelled results for angles of 45° and 90° are shown in Figs 16a and b respectively. The readings from thermocouples are triggered by the developed software in order to match the modelled to the experimental results. It is evident that the experimental results are lower in value than those from the model. There could be several reasons for this difference:

1. The model has several foregoing assumptions.
2. There is a difference between the conductivities of the high-temperature cement and workpiece material.
3. The readings from thermocouples are too slow to capture the rapid temperature changes.

In general, it can be concluded that the results of the model are in good agreement with the experimental date.

From these model verification procedures, it is proven that the model is set properly and, accordingly, reliable conclusions can be obtained from the model.
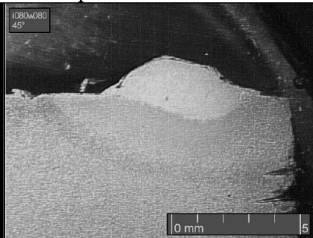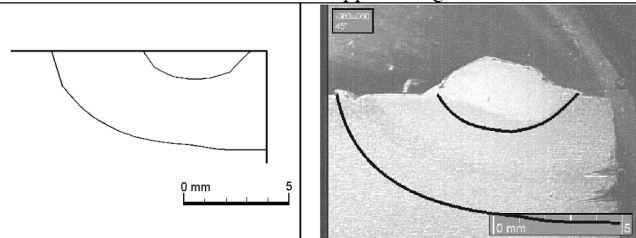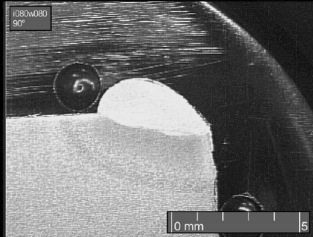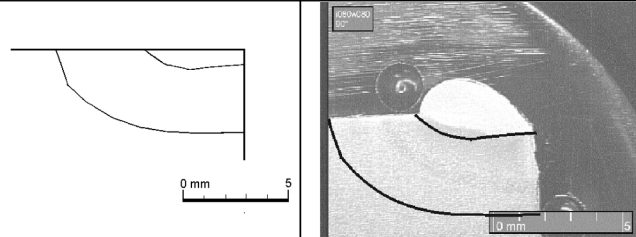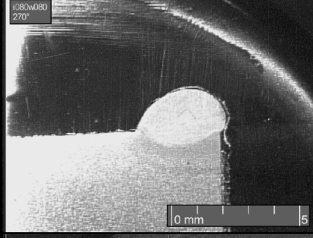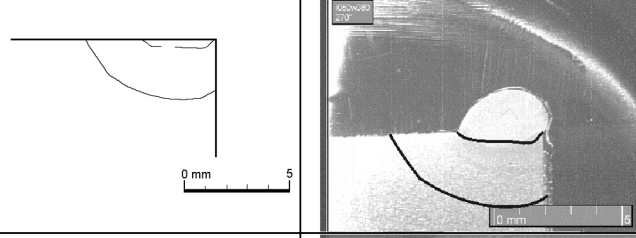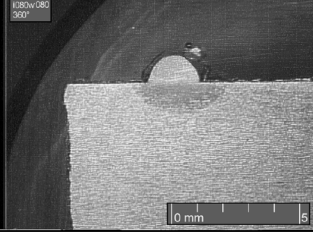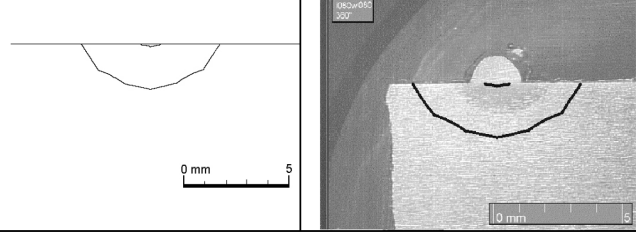
6 RESULTS AND DISCUSSION
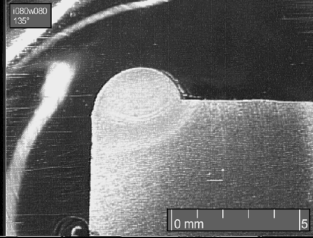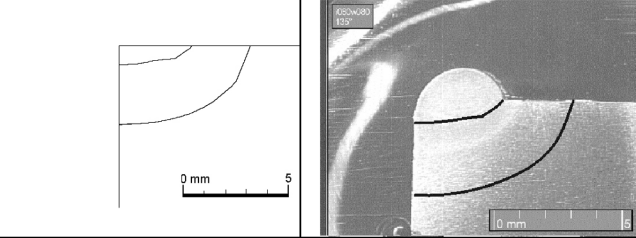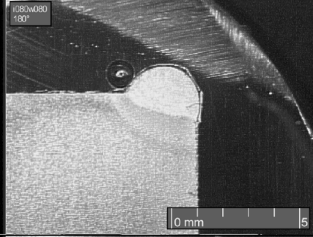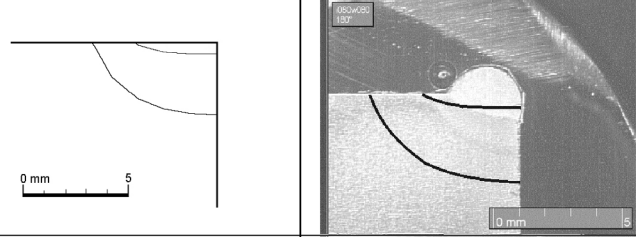
The developed model provides a better understanding of why fluctuations in the molten pool geometry at the top surface and HAZ occur when a constant heat input is used for the deposition of metal in the layers where heat transfer conditions differ at each point. This fluctuation is especially pronounced where metal is deposited along the external and internal boundaries of the workpiece. It is shown that the influence of the location of the bead on the welding parameters is an often-overlooked phenomenon. In general, the more complex the geometrical features of the previous layers, the more the heat-transfer conditions differ. To deposit successfully the layer of material with this technique, welding parameters have to be adjusted according to the geometry of the already-deposited layers. A solution of how to perform heat management for this technique is suggested.

A real-time adaptive controller of the heat input based on the obtained results is proposed. This feedforward controller is capable of adjusting the heat input in real time. The heat input is changed according to the underlying geometry. To take the environment into account (establish the relationship between the heat input and the part geometry) a new geometrical factor ξ_G is introduced. In the following, the mathematical method that derives a relationship between the heat input and the geometrical factor, summarized as $I = f(\xi_{GF})$, is presented. Once the level of the heat input is known, its value is updated. The rate of updating the heat input is synchronized with the welding speed by employing the data acquisition board.

6.1 Mathematical model

An accurate dynamic model [**39**] that provides guidance for sensing and corrective actions is needed for on-line adaptive control. The model provides a quantitative analysis of the thermal behaviour of the welding process and aids in a fundamental understanding of the influence of the welding current, the wire-feeding speed, the workpiece speed and the geometrical factor. An expression that will combine the net heat input, the wire-feeding

Table 2 Cross-sections and model predictions

	Process parameters: welding current I = 80 [A]; wire feeding speed v_F=80 [cm/min]		
	Experiment +	Model =	Overlapped Images
45°			
90°			
135°			
180°			
270°			
360°			

speed, the traverse speed and the heat conduction rate may be obtained by balancing the mass and energy flow through the control volume set around the molten pool, as shown in Fig. 17.

Segment A–A of the controlled volume is placed through the largest cross-sectional area of the liquid metal in the molten pool. By balancing the mass flow through the controlled volume, the maximum flowrate of the liquid metal may be calculated as the sum of the filler metal mass flowrate $\dot{m}_f$ (kg/s) and the maximum molten substrate flowrate $\dot{m}_w$ (kg/s). Then, the balance of energy at steady state is

$$\dot{m}_f h_0 + \dot{m}_w h_0 + \dot{Q}_{in} = (\dot{m}_f + \dot{m}_w)h_{liq} + \dot{Q}_k \qquad (10)$$
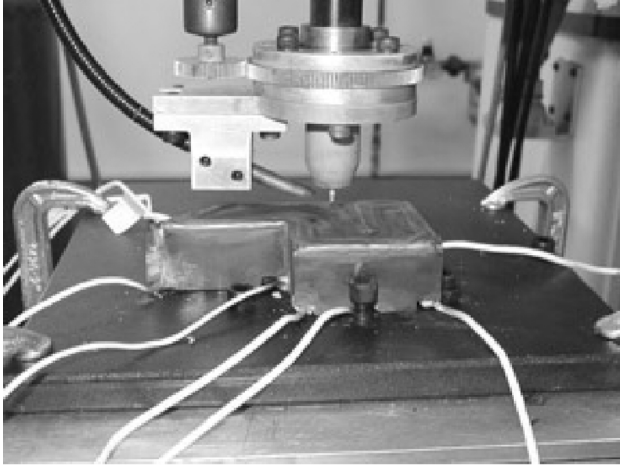
Fig. 14 Embedded thermocouples

where h_0 (J/kg) is the specific enthalpy of the filler metal, and the substrate metal entering the controlled volume, h_{liq} (J/kg) is the specific enthalpy of the liquid metal leaving the control volume, $\dot{Q}_{in}$ (W) is the net-heat input and $\dot{Q}_k$ (W) is the conduction heat flowrate

through the substrate. The balance can be rewritten as

$$\dot{Q}_{in} = \dot{Q}_f + \dot{Q}_w + \dot{Q}_k \tag{11}$$

The net heat input $\dot{Q}_{in}$ is used for melting the filler metal [$\dot{Q}_f$ (W)], for melting the substrate material [$\dot{Q}_w$ (W)] and for the heat dissipated by conduction, $\dot{Q}_k$. The heat used for heating and melting the filler metal is calculated as

$$\dot{Q}_f = \dot{m}_f(h_{liq} - h_0) = \frac{d_f^2 \pi}{4} v_f(\bar{h}_{liq} - \bar{h}_0) \tag{12}$$

where d_f (m) is the filler-wire diameter, v_f (m/s) is the filler-wire velocity and $\bar{h}_{liq} - \bar{h}_0 = 12 \times 10^9 \, \text{J/m}^3$ for carbon steel. The heat flowrate used to heat and melt the substrate material, $\dot{Q}_w$, is

$$\dot{Q}_w = \dot{m}_w(h_{liq} - h_0) = \dot{v}_w(\bar{h}_{liq} - \bar{h}_0) \tag{13}$$

where $\dot{v}_w$ (m^3/s) is the volumetric flowrate of the molten substrate metal. The net heat input $\dot{Q}_{in}$ can be determined accurately from the well-known relationship
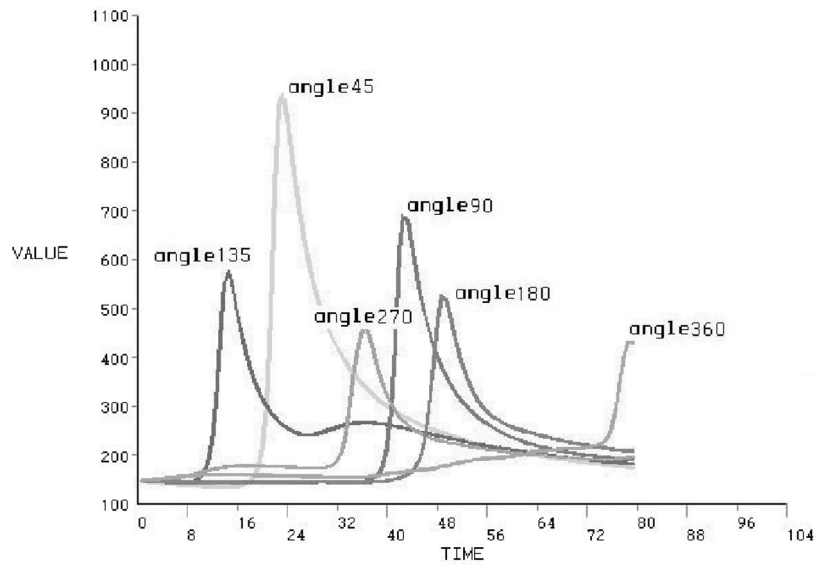
$$\dot{Q}_{in} = \eta_{arc}EI \tag{14}$$
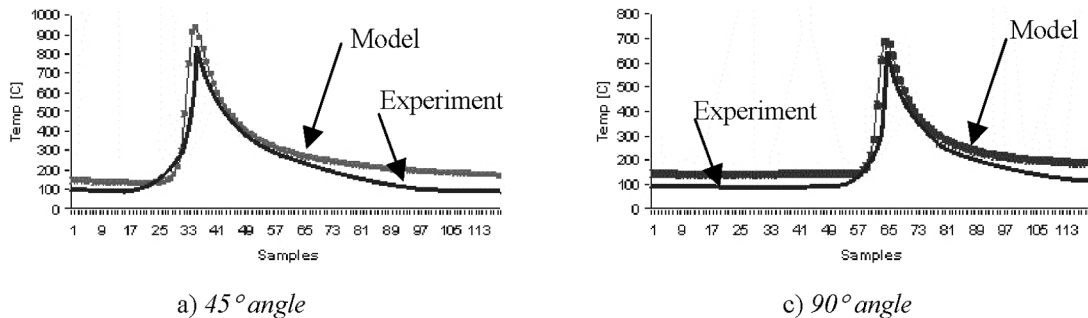

Fig. 15 Temperature history

a) *45° angle*   c) *90° angle*

Fig. 16 Experimental versus modelling temperature history
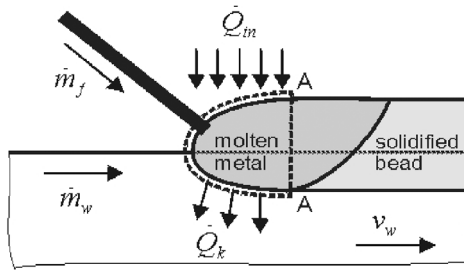
Fig. 17 Control volume

Fig. 18 Workpiece cross-section

where E (V) is the voltage and I (A) is the current measured from the process, and η_{arc} is the arc efficiency (equal to 0.7 for GTAW of mild steel). Based on the measurements,

$$E = b_0 + b_1 I \tag{15}$$

where $b_0 = 7.592$ and $b_1 = 0.02117$. The heat conduction rate at the surface is derived from $\dot{Q}_k(\tau) = kA(T_{liq} - T_0)/\sqrt{\pi\alpha\tau}$, where $A = w_b^2\pi/4$, and, after recognizing the Fourier number and correcting the expression to fit measured data, $\dot{Q}_k$ can be represented as [39]

$$\dot{Q}_k = 2.217\xi_G \frac{\alpha^2}{v_w}(\bar{h}_{liq} - \bar{h}_0)\left(\frac{w_b v_w}{2\alpha}\right)^{0.9666} \tag{16}$$

where α is the temperature diffusivity and w_b is the bead width. After substituting equation (15) into equation (14) and reorganizing the obtained expression, the net heat input used to calculate the welding current can be represented as

$$I = \frac{1}{2b_1}\left(\sqrt{b_0^2 + \frac{4}{\eta_{arc}}b_1\dot{Q}_{in}} - b_0\right) \tag{17}$$

where $b_0 = 7.952$ and $b_1 = 0.02117$ are non-dimensional, experimentally obtained constants [39]. The value for $\dot{Q}_{in}$ is obtained from equation (11) and substituted into known values from equations (12) to (14). The final equation (17) is further used for updating the heat input. To recapitulate, firstly, a three-dimensional solid model should be designed and digitized into the matrix of voxels, then the geometrical factors are calculated for each point and, finally, the welding current is calculated for the same point and its value updated. It should be noted that the whole calculation procedure is done off line, which virtually suppresses any possibility of delay in the heat input updating. As the result of this method, the heat input will be adjusted for every possible condition, i.e. the 'optimal process parameters' will be applied at every instance during the process of deposition. Here, the optimal process parameters can be defined as which usage leads to the deposition of smooth layers that are void free and above which the
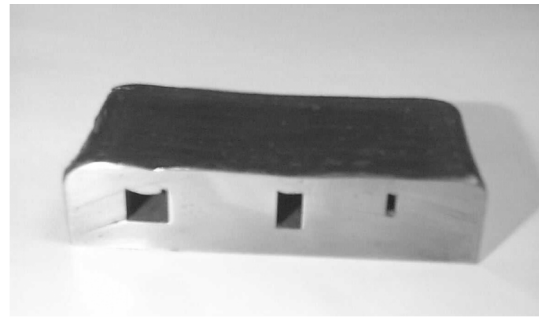
next layer can be deposited without introducing the milling process.

Results of the depositing material in layers over three channels can be observed in Fig. 18. However, before depositing the metal over the channels it was necessary to cover them with thin metal sheets in order to maintain conditions needed to sustain the arc. This was very easy to achieve since the computer numerically controlled machine used to mill the channels off was used to offset the path and to cut out covers of the exact size. These covers were not taken into consideration by the heat transfer model. Although these covers are made out of 1 mm thin sheets they were not burnt through because the heat input was significantly reduced. The heat input was calculated to melt only the incoming wire. This process is very dynamic, and the changes in the heat input are dictated purely by the complexity of the substrate geometry. The signals of the current and the voltage are recorded by sensing through the arc. The signals are shown in Fig. 19. Better insight into this procedure can be obtained if the results shown in Fig. 19 are compared with calculated heat input values shown in Fig. 4. It should be noted that, in the intervals where the calculated geometrical factor has zero values, the real value of the current is *not* zero. That value presents sufficient energy for melting only the filler metal but not the cover, and it is taken into account through the expression for the heat conduction dissipation. This method has a clear advantage in that it is independent
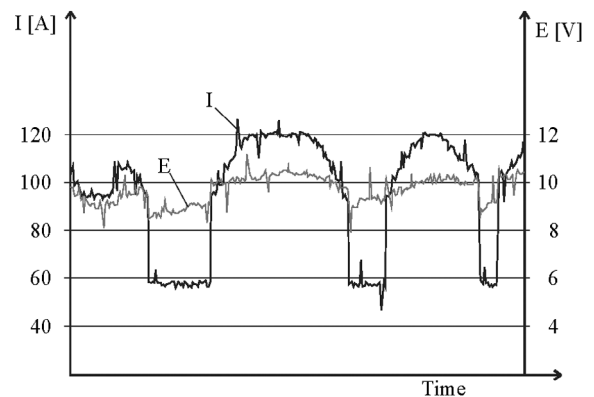

Fig. 19 Values of the welding current and voltage as functions of the geometry of the substrate

of the geometry, which is exactly what is needed for SFF based on GTAW. It can be applied in the same way for all conditions. It treats inside and outside edges, corners and channels equally. To the present authors' knowledge, this high level of the applicability has not been demonstrated by any of the previous methods.

7 CONCLUSION

A three-dimensional finite element model of the transient temperature-dependent heat transfer problem has been developed. This model provides a better understanding of the fluctuations of the size of the molten pool and HAZ that appear when a constant heat input is applied during the deposition process. The temperature fields are shown for the 'critical' angles. For these angles, the temperature history from the model is recorded and verified with the experimental results obtained from the embedded thermocouples. In addition, the model's results are verified through monitoring the experiments with a coaxially integrated CCD camera. With this camera, the molten pool geometry at the top surface is obtained and compared with the model's results. Moreover, the modelling results are verified experimentally by depositing beads under conditions similar to the conditions used in the model. Then, the beads are cross-sectioned, polished and etched. Images of the obtained cross-sections are compared with the results obtained from the model. The overall conclusion after all verification procedures are examined is that the modelling results are in very good agreement with the experimental results and, thus, the model can be safely used to predict process behaviour.

A conclusion derived from the model's results is used to develop a controller based on the newly introduced geometrical factor. Firstly, the expression is obtained by balancing the mass and energy flow through the control volume set around the molten pool. Then, the geometrical factor is introduced in the expression for the heat conduction rate. In the final step, the net heat input is used to calculate the welding current. A new feedforward controller that uses a calculated welding current (heat input) for heat management is developed. The overall system performance is monitored and recorded by sensing through the arc. Also, the controller demonstrated its versatility and robustness by effectively following the dynamic changes in the volume of the substrate, i.e. by updating the heat input so that the feeding material was successfully deposited.

ACKNOWLEDGEMENT

REFERENCES

1 Prinz, F. B. and **Weiss, L. E.** Method and apparatus for fabrication of three-dimensional metal articles by weld deposition. US Pat. 5,207,371, 1993.

2 Kmecko, S. I., Kovacevic, R. and **Jandric, Z.** Machine vision based control of gas tungsten arc welding for rapid prototyping. In Proceedings of the 11th Annual Solid Freeform Fabrication Symposium, Austin, Texas, 2000, pp. 578–584.

3 Jandric, Z. and **Kovacevic, R.** New way of process parameters optimization in SFF based on deposition by welding. In Proceedings of the 12th Annual Solid Freeform Fabrication Symposium, Austin, Texas, 2001, pp. 110–119.

4 Baker, R. Method of making decorative articles. US Pat. 1,533,300, 1925.

5 Kovacevic, R. Rapid manufacturing of functional parts based on deposition by welding and 3D laser cladding. In Procedures of the MoldMaking Conference, 3–5 April 2001, pp. 263–276 (presented by the MoldMaking Technology Magazine).

6 Mort, D. and **Hood, B.** Apparatus for continuously cladding a dished surface. US Pat. 4,149,061, 1979.

7 Million, K. and **Zimmermann, H.** Method and apparatus for manufacturing a tube bend metal. US Pat. 4,517,434, 1985.

8 Bronowski, H. Device for building up a workpiece by deposit welding. US Pat. 4,621,762, 1986.

9 Million, K. and **Zimmermann, H.** Method of preparing structural components having a symmetrically curved wall by buildup welding. US Pat. 4,671,448, 1987.

10 Edmonds, D. P. and **McAninch, M. D.** Method and apparatus for building a workpiece by deposit welding. US Pat. 4,775,092, 1988.

11 Doyle, T. E., Edmonds, D. P., McAninch, M. D. and **Ryan, P. M.** Method and apparatus for building a workpiece by deposit welding. US Pat. 4,842,186, 1989.

12 Buhrmaster, C. L., Clark, D. E. and **Smartt, H. B.** Apparatus for gas–metal arc deposition. US Pat. 5,052,331, 1991.

13 Prinz, F. B. and **Weiss, L. E.** Method and apparatus for fabrication of three-dimensional metal articles by weld deposition. US Pat. 5,207,371, 1993.

14 Aleshin, S. Method for depositing material on the tip of a gas turbine engine airfoil using linear translational welding. US Pat. 5,160,822, 1992.

15 Schneebeli, F., Braun, O., Tanner, B. and **Dekumbis, R.** Method of production of workpieces by welding equipment. US Pat. 5,233,150, 1993.

16 Spencer, J. D. and **Dickens, P. M.** Production of metal parts featuring heavy sections using 3D welding. In Proceedings of the 1st National Conference on *Developments in Rapid Prototyping and Tooling* (Ed. G. Bennett), Buckinghamshire College, 1995, pp. 127–137.

17 Norman, R. D. and **Dickens, P. M.** 3D welding fabrication: strategies for sloped surfaces. In Proceedings of the 1st National Conference on *Developments in Rapid Prototyping and Tooling* (Ed. G. Bennett), Buckinghamshire College, 1995, pp. 51–65.

18 Ribero, D. A. and **Norrish, J.** Rapid prototyping process using metal directly. In Proceedings of 7th Solid Freeform Fabrication Symposium, 1996, pp. 249-256.

19 Ksiazkiewicz, R. and **Gustafson, N.** Robotic GTAW may prove key to higher gas turbine engine production. *Weld. J.*, December 1996, **75**(12), 33–37.

20 Krause, F. L., Ciesla, M., Stiel, C. and **Ulbrich, A.** Enhanced rapid prototyping for faster product development processes. *Ann. CIRP*, **46**(1), 93.

21 Song, Y. A., Park, S., Hwang, K., Choi, D. and **Jee, H.** 3D welding and milling for direct prototyping of metallic parts. In Proceedings of the 9th Solid Freeform Fabrication Symposium, Austin, Texas, 1998, pp. 495–501.

22 Kovacevic, R. and **Beardsley, H. E.** New rapid prototyping technique based on 3-D welding. In Proceedings of the 31st CIRP International Seminar on *Manufacturing Systems*, May 1999, technical paper PE99-126, pp. 1–5 (Society of Manufacturing Engineers, Dearborn, Michigan).

23 Jandric, Z., Kmecko, I. S. and **Kovacevic, R.** Dynamic modeling of GTAW for rapid manufacturing. In Proceedings of the 11th International Conference on *Computer Technology in Welding*, NIST Special Publication 973, Columbus, Ohio, 5–9 December 2001.

24 Rosenthal, D. The theory of moving sources of heat and its application to metal treatments. *Trans. ASME*, 1946, **68**(11), 849–866.

25 Rykalin, N. N. *Calculation of Heat Process in Welding*, 1960 (Mashgiz, Moscow).

26 Friedman, E. Thermodynamic analysis of the welding process using the finite elements method. *Trans.* ASME, *J. Pressure Vessel Technol.*, **97**, 206–213.

27 Rykalin, N. N. and **Nikolaev, A. V.** Welding arc heat flow. *Weld. World*, 1971, **9**(3–4), 112–132.

28 Pavelic, V. Weld puddle shape and size correlation in a metal plate welded by the GTA process. In *Arch. Physics and Weld Pool Behaviour: An International Conference*, The Welding Conference, 1979, pp. 251–258.

29 Beuth, J. L. and **Narayan, S. H.** Residual stress-driven delamination in deposited multi-layers. *Int. J. Solids Structs*, 1996, **33**(1), 65–78.

30 Hu, Z., Labudovic, M., Wang, H. and **Kovacevic, R.** Computer simulation and experimental investigation of sheet metal bending using laser beam scanning. *Int. J. Mach. Tools Mf.*, 2001, **41**, 589–607.

31 Bonifaz, E. A. Finite element analysis of heat flow in single-pass arc welds. *Weld. J.*, May 2000, **79**(5), 121s–125s.

32 Kamtekar, A. G., Little, G. H. and **Ji, T.** An efficient finite element model for calculating transient temperatures during welding. Part I: procedure. *Computer Modeling and Simulation in Engng: CMSE*, 1998, **3**(2), 75–86.

33 Little, G. H., Ji, T., Kamtekar, A. G. and **Bani, S. B.** An efficient finite element model for calculating transient temperatures during welding. Part II: applications. *Computer Modeling and Simulation in Engng: CMSE*, 1998, **3**(2), 87–97.

34 Radaj, A., Christensen, N., DuPont, J. N. and **Marder, A. R.** Thermal efficiency of arc welding process. *Weld. J.*, December 1995, **74**(12), 406s–416s.

35 Myers, P. S., Uyehara, O. A. and **Borman, G. L.** Fundamentals of heat flow in welding. *Weld. Res. Counc. Bull.*, July 1967, **123**.

36 Brown, S. B. and **Song, H.** Implications of three-dimensional numerical simulations of welding of large structures. *Weld. J.*, 1992, **71**(2), 55s–62s.

37 Kim, C. S. Technical Report ANL-75-55, Argonne National Laboratory, Argonne, Illinois, 1994, pp. 1–24.

38 Kamala, V. and **Goldak, J. A.** Error due to two dimensional approximation in heat transfer analysis of welds. *Weld. J.*, September 1993, **72**(9), 440s–446s.

39 Kmecko, I. S., Jandric, Z. and **Kovacevic, R.** Influence of geometrical factor on heat conduct rate during GTAW for welding-based deposition. In Proceedings of the ASME Symposium on *Nontraditional Manufacturing Research and Application*, New York, 11–16 November 2001 (American Society of Mechanical Engineers, New York).